Materials and Design 159 (2018) 170–185

Contents lists available at ScienceDirect

Materials and Design

journal homepage: www.elsevier.com/locate/matdes

Full-field measurement with nanometric accuracy of 3D superficial displacements by digital profile correlation: A powerful tool for mechanics of materials

Luigi Bruno

Department of Mechanical, Energy and Management Engineering, University of Calabria, Via Bucci 44C, 87036 Rende, CS, Italy

HIGHLIGHTS

- Combined use of profilometry and digital image correlation for 3D displacement vector measurement
- Full-field and nanometric accuracy on displacement components
- Easy integration with commercial software for post-processing profilometry data

GRAPHICAL ABSTRACT

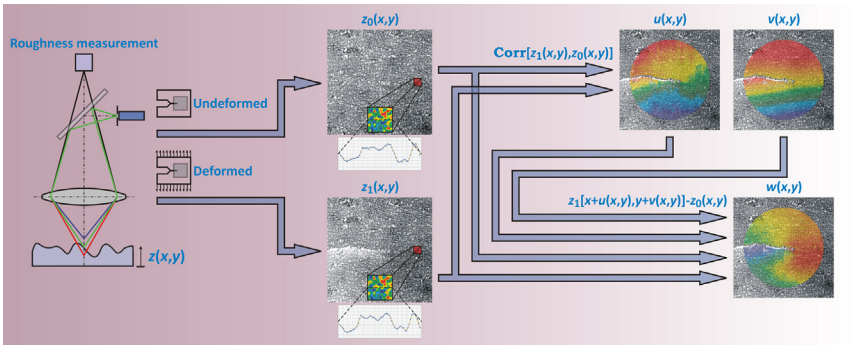

ARTICLE INFO

Article history:
Received 15 June 2018
Received in revised form 19 August 2018
Accepted 28 August 2018
Available online 29 August 2018

Keywords:
Digital image correlation
Profilometry
Full-field measurement
Confocal microscopy
Mechanics of materials

ABSTRACT

In recent decades, technological innovations have prompted the development of pioneering materials that attempt to satisfy new and forthcoming needs. The innovation in these materials is usually from their peculiar properties, which in many cases make them uniquely appropriate for a specific application. In this context, the development of innovative measurement techniques can provide more comprehensive understanding and knowledge of these materials' properties, often non-conventional and not easily retrieved by standard procedures. In order to obtain a full-field 3D displacement vector of a surface under investigation, the author proposes the combination of two well-known measurement techniques: the Confocal Microscopy (CM) and the two-dimensional Digital Image Correlation (2D-DIC). Specifically, CM has demonstrated its ability to successfully attain microscopic topography on a highly finished surface with sub-micrometric roughness, and such a technique could be used as a carrier to successfully apply the 2D-DIC algorithm. By this approach, it is not difficult to reach an accuracy of a few nanometers on the displacement measurement. The feasibility of the procedure proposed herein was demonstrated by two case studies: a tensile test of a Ni-alloy edge crack specimen, and a hardness test carried out on a thick AISI 1040 disk.

1. Introduction

The wide-reaching technological advances made over the last decades have allowed for the development and diffusion of a number of new materials [1–3]. This process of innovation is not an end in itself, but is being driven and accelerated by different needs, coming from several fields.

Engineers are perpetually trying to improve the performance of the mechanical properties with the aim of using them in increasingly critical and extreme applications – e.g. sports competitions, aerospace, energy,

E-mail address: luigi.bruno@unical.it.

https://doi.org/10.1016/j.matdes.2018.08.052
0264-1275/

defense and military [4]. Applications in electronics, computer science, and tailored sensors demand materials that accomplish specific tasks that are nonetheless contained to the greatest extent in weight and dimension [5]. Biomedical and biomechanical studies and research show the advantages of new materials used for their biocompatibility [6], capability to act as cure carriers [7], or capacities for inspecting [8]. In this framework, mechanical properties often represent a crucial aspect of design and development of these innovations, even if the primary aim has not been to satisfy specific stiffness and/or strength constraints.

Nowadays, the tools available to carry out experimental stress analysis are applied in several fields of mechanics of materials, covering a wide spectrum of analyses and serving numerous ends. It would be, as such, a daunting task to undertake a thorough classification of them all. It would result difficult, in fact, to merely list those that are most used or most popular. This lies beyond the scope of the present paper, in which, instead, the author intends to limit the focus on those techniques that are most typically used for measuring displacement field (i.e. mechanical strain) or material structure (i.e. microscopic imaging and profile). Among the methods suitable for studying the mechanical behavior of innovative materials, the most popular are those capable of performing full-field measurements, i.e. to extract a large amount of information on a significant portion of the material under investigation. This distinctive feature can play a key role when a material behaves in a non-conventional way, due to its heterogeneity and/or its complex structure.

Speckle interferometry [9] and digital holography [10] are two interferometric methods able to measure, in their basic configurations, a single displacement component with interferometric accuracy. The strengths of these techniques reside in their high sensitivity (few nanometers) and the ease of use of their recording media (CCD/CMOS cameras). On the other hand, the experimental setups are complex to assemble and manage, and their sensitivity to external disturbances is significantly high. On the contrary, digital image correlation (DIC) methods [11], sharing some of the strengths of the interferometric techniques (full-field capability, information recorded by cameras), allow for the acquisition of two (by the conventional 2D-DIC) or even all three (by the 3D-DIC arrangement) displacement components through much simpler experimental configuration and with a much smaller disturbance sensitivity. In contrast, the displacement sensitivity of DIC is much smaller (typically a few micrometers) and depends on displacement gradients and on the quality of the imaging process.

Instead of cameras, which are extremely useful for the aforementioned methods for measuring deformation, it is possible to use alternative imaging techniques that are capable of capturing the structure of the materials at a smaller scale, such as: Scanning Electron Microscopy (SEM) for reflection imaging of any opaque material, Transmission Electron Microscopy (TEM) for transmission imaging of thin film or transparent materials, Optical Coherence Tomography (OCT) for retrieving the structure of transparent tissues, and Electron BackScatter Diffraction (EBSD) for identification of crystal orientation, phases and defect.

Today, different types of profilometers are used to characterize the outer surface structure of a material, thanks to the wide applicability of this specific machine to characterize thickness, texture, roughness, thin films, coatings, semiconductor, wear, corrosion, and perform biomedical and biological analyses. The profilometers can be classified in two categories: stylus-based and light-based. The devices based on the stylus require a probe that follows the profile of the surface under test, according to different operating principles. In its most basic configuration, the interaction is purely mechanical. According to this concept, the first profilometers were built to measure roughness along a line, and even today they are profitably used in different applications to this end. Nevertheless, at present, significantly higher accuracy is attained by applying the scanning probe microscopy (SPM) method, which obtains the outer surface geometry by exploiting the interaction between the stylus and the surface under investigation at atomic level. Among the possible methods of implementation, the two most popular are the Scanning Tunneling Microscopy (STM) [12] and the Atomic Force Microscopy (AFM) [13]. On the other hand, the light-based devices have the advantage of preventing any contact between the measurement system and the surface under investigation. Among the several light-based implementation methods, the most successful are those based on White Light Interferometry (WLI) [14] and Confocal Microscopy (CM) [15]. The effectiveness of this type of analysis in material science [16–20] is demonstrated today by the numerous commercial apparatuses on the market that integrate these methods, available at increasingly reasonable prices.

The combined use of all of the aforementioned techniques can be found in a number of scholarly papers. Particularly common is the application of correlation algorithms to the various imaging system ways different form the conventional one – i.e. focusing an object on a sensor by way of an optical lens. This approach requires the acquisition of two configurations of the same portion of the surface under investigation, before and after the application of a deformation field. One of the most popular implementation techniques consists of applying the 2D-DIC on the images obtained by SEM, which measured and monitored deformations occurring, at a very low scale, in different type of materials [21–27]. Similar results can be attained through TEM [28] and EBSD [29]. In all these cases, the spatial resolution is much higher than that of conventional imaging systems. On the other hand, this equipment works in a vacuum, they are expensive, and they do not allow for the acquisition of the out-of-plane component of the displacement vector. This is due to the lack of information along the direction orthogonal to the plane containing the image. In addition, local contrast is often slightly different in the two loading configurations, decreasing the accuracy and reliability of the correlation algorithms. Consequently, bigger subsets have to be used for properly running DIC procedures, and displacement fields characterized by high gradients are retrieved with lower accuracy. In fact, it is worth noting that when correlation algorithms are successfully applied to the images acquired by these techniques, the subset size is hardly smaller than $40 \div 50$ pixels, and the displacement fields are considerably regular.

The specific case of the combined use of OCT and DIC [30,31] deserves different consideration. In this case, spatial resolution is comparable to those techniques based on a conventional imaging system, and when different configurations are considered, the decay of image quality is even worse than that occurring in electron scanning techniques. Nevertheless, it works for biological materials, and has acted as a useful investigation tool in different medical fields. In addition, thanks in large part to its capacity to penetrate through tissues of the light sources used by OCT machines, the images can be analyzed by complex correlation algorithms that are able to retrieve volume deformations, rather than simply planar ones – i.e. Digital Volume Correlation (DVC) [32].

The SPM methods display similar spatial resolution to that of electron scanning techniques, and suffer less local contrast loss, thanks to the fact that the imaging operation is not performed by lens, but consists of a digital representation of the physical topography of the surface under investigation, shown at nanometric scale. In addition, SPM methods can retrieve the out-of-plane component, thanks to the topographic information provided by the measurement method. Vendroux et al. in 1998 [33–35] published a series of three papers by which they proposed the combined use of profilometry and DIC to retrieve displacement vectors, with particular emphasis on the STM; in their research, the authors proposed the idea, carried out an extensive analysis of DIC procedures, and reported some preliminary experimental results.

A combination of AFM and DIC was used by a research group of University of South Carolina for some applications: in-plane mechanical characterization of polymeric thin film [36], compensation of AFM in-plane distortion due to the translation stage of the device [37], and the mapping of nanoscale wear occurring on a gold coating [38]. Other interesting applications of this method in the field of mechanics of

materials include residual stress measurement [39], elastic characterization of MEMS [40], and identification of fracture mechanics parameters of a silicate glass at nanoscale [41]. In all these cases, the nanometric resolution of the AFM device allows for the in-plane displacement components to be determined by correlation algorithms with sub-nanometric resolution. However, the out-of-plane component was usually neglected. In particular, in the case of wear evaluation [38], the consumption of the materials – i.e. the lowering of the peak – was evaluated by analyzing the correlation coefficient and comparing profiles along the same segment of the gold coating. Instead, when applying this approach to an analysis of displacement field around the crack tip of a silicate glass [41], all three displacement components were retrieved. In this application, a specific analytic model was assumed according to the elastic solution for linear-elastic materials, which required the estimation of a limited number parameters by means of an optimization process. This approach is known as the Integrated Digital Image Correlation (I-DIC) method, the assumptions of which do not necessarily involve kinematic variables – i.e. displacement field. Additional and alternative parameters can be included in analytical models in order to retrieve the displacement components. These can include the stress intensity factor and the residual stress state or any mechanical property (e.g. Young's modulus, Poisson's ratio, yield strength, hardening coefficient), all of which significantly impact the mechanical response.

Correlation procedures, and in particular the Global Digital Image Correlation method (GDIC) [42], were also applied to the profiles retrieved by CM. The GDIC approach is based on the definition of a mesh on the surface of the specimen and an algorithm applied iteratively to identify displacement components. The Eindhoven research group of TUE, together with other colleagues, developed a series of outstanding applications obtained through the combined use of GDIC and CM profile data. Van Beeck et al. [43–45] studied 3D deformations of polymer-coated metals induced by metal sheet stretching. The procedure consisted of non-standardized dog bone samples analyzed by a micro-tensile machine; displacement component maps and profiles were obtained at different points on the specimens. Bertin et al. [46] performed a micro-mechanical characterization of a two-grains, low-carbon interstitial free steel specimen subjected to a tensile test. Kleinendorst et al. [47] demonstrated how to study complex geometries through a procedure based on adaptive mesh by which they successfully retrieved the displacement field on an S-shaped stretchable electronic part. Through a similar experimental approach, the local curvature of a bulged membrane [48] was measured, as was a micro-beam under bending loads [49] on parts designed for MEMS applications. In the last application, the specimen's profile was measured by Dual Wavelength Digital Holographic Microscopy (DWDHM) and the entire procedure showed a curvature resolution of 1.5×10^{-6} μm^{-1}. Another novel application obtained through the combination of DIC and CM analyses is reported in [50], in which the authors carry out an extensive study of dislocation mechanisms in austenitic stainless steel due to stress corrosion cracking.

In the present paper, the author will demonstrate how to profitably combine CM and DIC in the field of mechanics of materials. It is done with the aim of exploiting the strength of this approach, while proposing a method capable of measuring the whole 3D displacement field with an accuracy that is satisfactory for several applications. More specifically, the use of CM provides nanometric accuracy and eliminates the need to work in a controlled environment, as is required by SEM, TEM and EBSD. CM can retrieve out-of-plane information, as shown in [43,46–49], that electron-scanning techniques are not able to obtain. In addition, such electron scanning techniques are also prone to defocusing concerns. In contrast with SPM techniques, with CM there is no required contact between a probe and the surface, which could damage or alter a weak specimen.

In addition to the benefits of CM, the author shows how a commercial DIC algorithm can be successfully applied to process images without the need of any assumption on the displacement field, as required by I-DIC, or by a FEM-like mesh definition, as in G-DIC. The fact that nothing should be assumed in order to retrieve all three displacement components offers the flexibility to manage any displacement field occurring on the surface of the specimen. Hence, a non-kinematically compatible deformation field can also be measured without knowing a priori any information about its spatial distribution – e.g. displacement around a crack tip. Thanks to the high sensitivity of the profilometer (about 10 nm), the spatial carrier necessary to make the DIC algorithm work – i.e. the surface roughness – can show an extremely low contrast, and the subset size can be chosen small enough ($15 \div 25$ pixels) to retrieve displacement fields characterized by steep gradients. Through this procedure, it was possible to obtain an accuracy of approximately 10 nm for all three displacement components, even if a standard confocal microscope was used.

The proposed procedure was tested in two case studies. The first case study consists of the measurement of the displacement field around the crack tip of a Ni-alloy specimen under uniaxial tensile load. In this case, the correlation algorithm is able to identify displacements on the entire sample area, given that essentially the entire surface area is subject to elastic deformations that do not significantly alter the roughness. As such, almost every portion of the area is able to correlate after the deformations occur. In the second case, the 3D displacement field around the indentation obtained by a standard Brinell test on an AISI 1040 steel specimen was measured. This test emphasized how high plastic strains occurring on the area where the indentation is applied cause the DIC algorithm to fail, while the same algorithm worked soundly just beyond the indentation area, where the displacement gradients (for all the three components) were clearly retrieved by the correlation algorithms.

2. Materials and methods

The method proposed by the present paper requires the measurement of the topography of a surface with nanometric accuracy, and the post-processing of the 3D information by a reliable 2D-DIC algorithm.

The first task can be accomplished with many types of profilometer. The author used the Anton Paar [51] profilometer, which is part of an instrumented indentation station formed by four machines: an optical microscope, the microindentation tester (MHT), the nanoindentation tester (NHT), and the confocal profilometer (ConScan).

The operating principle of this specific profilometer is based on the chromatic aberration principle. As shown in Fig. 1, a white light source is focused on the surface under investigation by a lens. Due to the dispersion effect, each wavelength is focused at a different distance, hence the spectral content of the light diffused by the illuminated point is quite narrow and can be used for encoding the *z*-coordinate. To increase sensitivity to this signal, the light coming from the object is focused on the spectrometer sensor by a pinhole.

The measurement range depends on the amount of aberration. In the case of the device used in this work, it is 400 μm. The accuracy provided by this profilometer in the *z* direction is 10 nm, but it can be significantly improved (sub-nanometric) by using more sophisticated devices. Like most profilometers, the one used in this test works by scanning the surface specimen. Precision in the *x* and *y* directions depends on the accuracy of the translation stage, which is piezo-actuated, with an accuracy of 10 nm and a measurement range of several centimeters in both the *x* and *y* directions. This accuracy can be significantly improved (sub-nanometric) if the measurement range of the translation stage is smaller. In fact, due to the small size of the inspected surface, a few millimeters are usually enough. By contrast, the indentation station used in the present work needs much bigger displacement to move the specimen between the different machines.

For the acquisition of a surface topography, it is necessary to define the dimension and number of sampling points in both the *x* and *y* direction. Some additional settings can be chosen, such as the acquisition

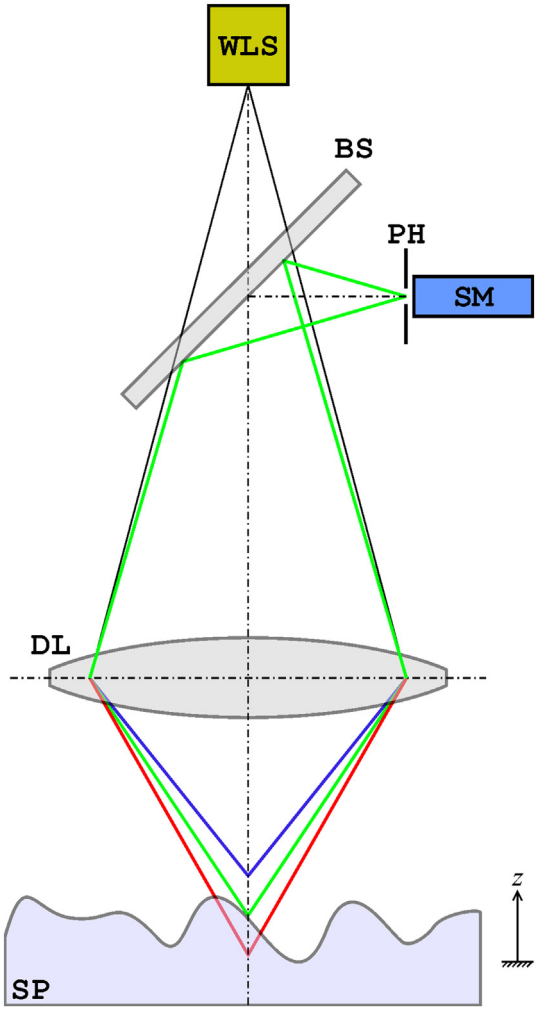

Fig. 1. Operating principle of a confocal profilometer based on chromatic aberration: WLS, white light source; BS, beamsplitter; PH, pinhole; SM, spectrometer; DL, dispersive lens; SP, specimen.

frequency, the data averaging, and the starting point within the measurement range.

The post processing of the profile data was carried out by the commercial DIC software VIC-2D (version 2009.1.0, build 933) distributed by the Correlated Solutions, Inc. [52]. There are two basic parameters used to launch the correlation procedure to evaluate the (in-plane) horizontal $u(x,y)$ and vertical $v(x,y)$ displacement components: the subset and the step. Both parameters are integers defined in pixels, whose dimensions depend on how the image is digitalized.

If the image is acquired in the conventional way (focused on a sensor by a lens), the pixel dimension is determined by the magnification ratio – i.e. lens focal length and the distance between the lens and the sensor. In this case, the distortions of the lens can introduce a systematic error into the DIC procedure. Instead, as is the case of the proposed procedure, when the pixel intensity is coded by the z-coordinate of the generic point, its transversal dimension depends on the scanning procedure adopted during the profile acquisition.

The subset dimension is crucial for the successful application of the DIC procedure. It defines the extension of the area around the generic pixel to be used while searching for its new location among the other images acquired in the experiment; normally, it is an odd number of pixels, in order to assign displacement components found by the correlation procedure to the central pixel. The subset should be big enough to include a certain number of image features, which allow the correlation algorithm to function properly. Normally, the application of an autocorrelation procedure on a single image allows the average size of the features to be determined, which can in turn be assumed as the minimum dimension of the subset. In addition, this dimension should be small enough to avoid averaging the displacement gradients, which would definitely introduce a bias to the measurements. The importance of this choice of parameters is confirmed by the high number of studies that have been carried out on this specific issue, which has yet to be resolved [53,54].

The size of the step determines how the images to be analyzed will be sampled, and it specifies how many pixels to skip during the DIC analysis. Normally, this impacts only the complexity of the calculation, not the quality of the results. In theory, if it is set to a size smaller than the subset, the operator is requiring an oversampling of the experimental data. In fact, in such a case the DIC algorithm will try to find the displacement of points correlated between them. Nevertheless, light oversampling sometimes simply provides additional information, which allows for a smoother distribution of the displacement fields without significantly affecting the processing time.

The proposed procedure was tested on two different loading configurations:

1. A customized Ni-alloy edge crack thin plate subjected to a tensile test;
2. An AISI 1040 thick disk subjected to a Brinell indentation test.

The first test was carried out completely under the profilometer, exploiting a linear translation stage actuated manually and capable of expanding symmetrically along the control direction (Fig. 2a). The use of this type of translation stage is ideal, as it compensates for the rigid body motions occurring during the application of the tensile load,

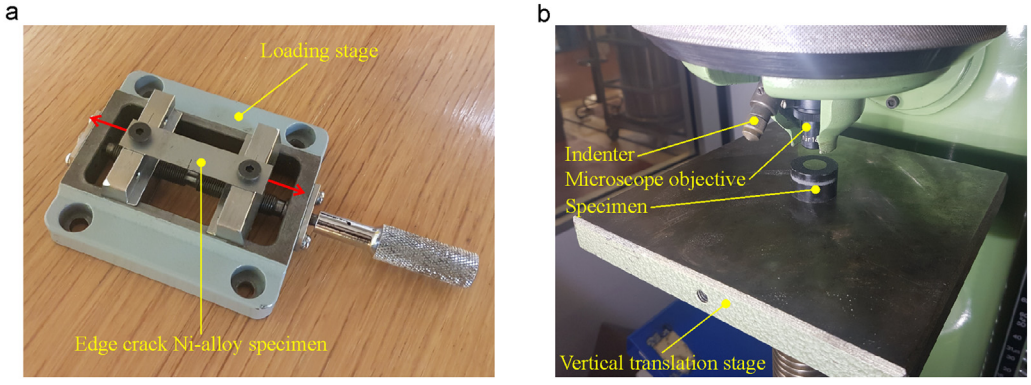

Fig. 2. Specimens used for testing the measurement procedure: a) edge crack Ni-alloy specimen subjected to a tensile load manually applied by a uniaxial loading stage; b) AISI 1040 specimen disk hot-mounted in a resin and placed on the vertical translation stage of an indentation testing machine.

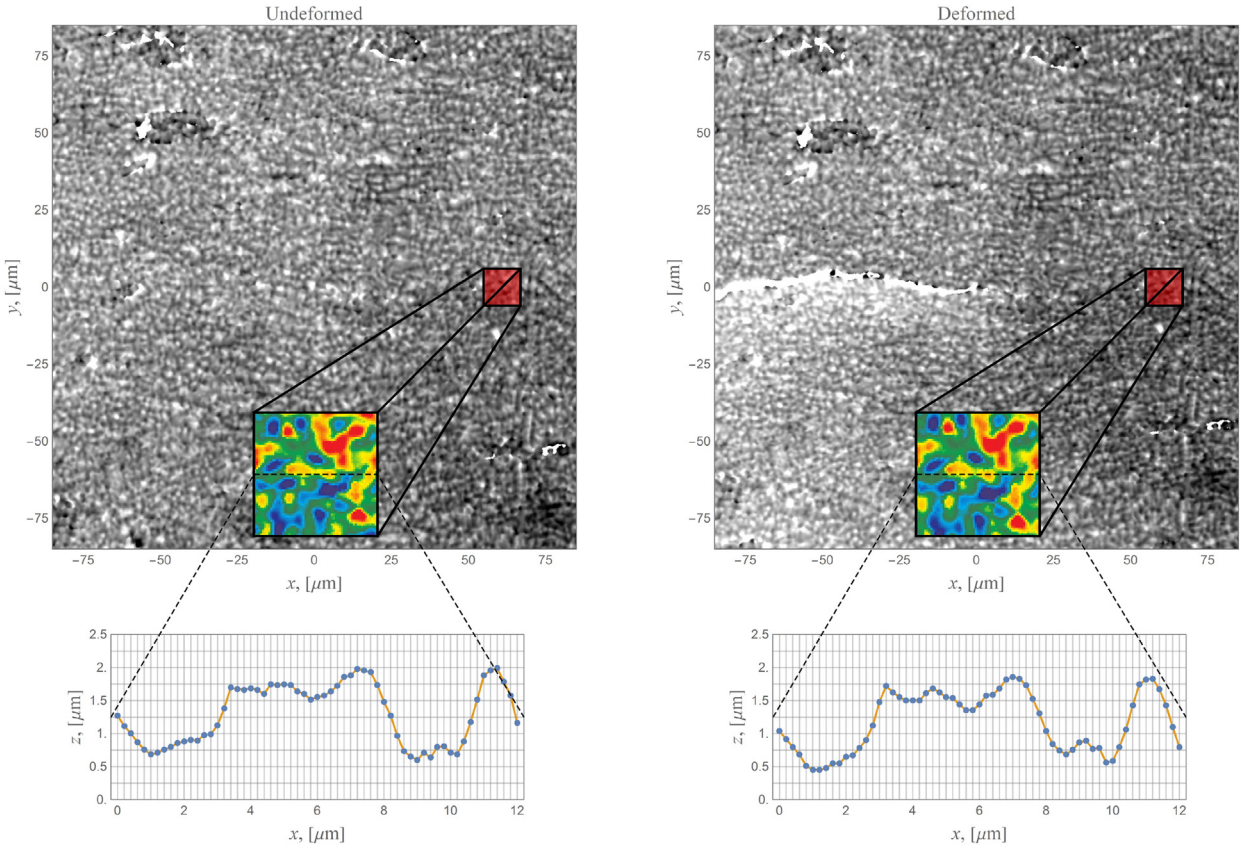

Fig. 3. The profiles (in grayscale representation) of the Ni-alloy in the undeformed (left side) and deformed (right side) configurations. A portion of a specific area is highlighted (red semitransparent box) and magnified (color density box) in both configurations. In the lower row of the figure, the topography along the horizontal centerline of the highlighted area is represented with a further magnification, and the location of sampling points is evidenced by the vertical grid lines. (For interpretation of the references to color in this figure legend, the reader is referred to the web version of this article.)

minimizing the translation of the Region Of Interest (ROI) along the loading direction.

For this specimen, a square ROI of 200 μm × 200 μm was chosen, and it was sampled by 1000 × 1000 acquisitions. It means that the distance δ between two adjacent points (in *x* or *y* direction), whose *z*-coordinate was acquired, is equal to 0.2 μm. This choice is fundamental in this type of analysis, because it affects the accuracy of the displacement measurement taken during the procedure. It has to be small enough to catch the peaks and the valleys, drawing a 3D profile of the surface. This is the structure that allows the correlation algorithm to perform a successful analysis. If the value for δ is too high, instead, this implies an under-sampling of the profile and consequently a random structure of it that cannot be used as a carrier for the correlation procedures. Obviously, there is a limit to how small δ can be fixed. First, the piezoelectric translation stages used to scan the surface has a resolution under which they are no longer reliable. Secondly, the lower the value of δ the higher the acquisition time for a fixed ROI dimension. Finally, there is no need to oversample the profile of the surface under investigation, as it does not improve the accuracy of the DIC analysis.

Fig. 3 shows the surface profile of the edge crack Ni-alloy specimen acquired before (left side) and after (right side) the application of the tensile load. In the figure, the topography is represented by a grayscale image with lower and upper bounds chosen in order to provide a good representation. It is possible to see the crack opening in the deformed configuration. The red semitransparent box highlighted on the two profiles represents the same area (12 μm × 12 μm, i.e. 60 pixels × 60 pixels) before and after the application of the load. This area is then magnified in the lower-central area of the profile and represented by a proper color function to show how the structure is maintained after deformations occur in the ROI. In the lower row, the topography measured along the horizontal centerline of this area is reported in order to demonstrate how the profile is sampled and how small the changes in the two configurations are. The profiles in the two configurations are analyzed by the 2D-DIC software, which will extract the two in-plane displacement components $u(x,y)$ and $v(x,y)$. The results are reported and discussed in the following sections, while the roughness parameters are calculated and shown in Table 1.

The second test was carried out on an AISI 1040 disk (15 mm diameter, 10 mm thickness) hot-mounted in a thermoplastic resin by a Struers mounting press (model CitoPress-1). After the mounting operation, the specimen surface was polished according to the vendor protocols for this specific material. Polishing was performed by a Struers grinding/polishing machine (model Tegramin-25) and the final specimen is the aforementioned disk mounted in the black resin disk (25 mm diameter, 30 mm thickness) shown in Fig. 2b.

This type of specimen was subjected to a Brinell hardness test on a manual Wolpert universal tester, which consisted in applying a load of 2 kg with a spherical indenter of 1 mm diameter. In Fig. 2b it is possible

Table 1
Roughness parameters of the specimens.

	Specimen 1, Ni-alloy Tensile test on edge crack plate	Specimen 2, AISI 1040 Brinell indentation test
Ra [μm], average	0.532	0.084
Rq [μm], root mean square	0.666	0.106
Rt [μm], maximum height	3.195	0.535
Rsk, skewness	0.358	0.245
Rku, kurtosis	3.012	3.089

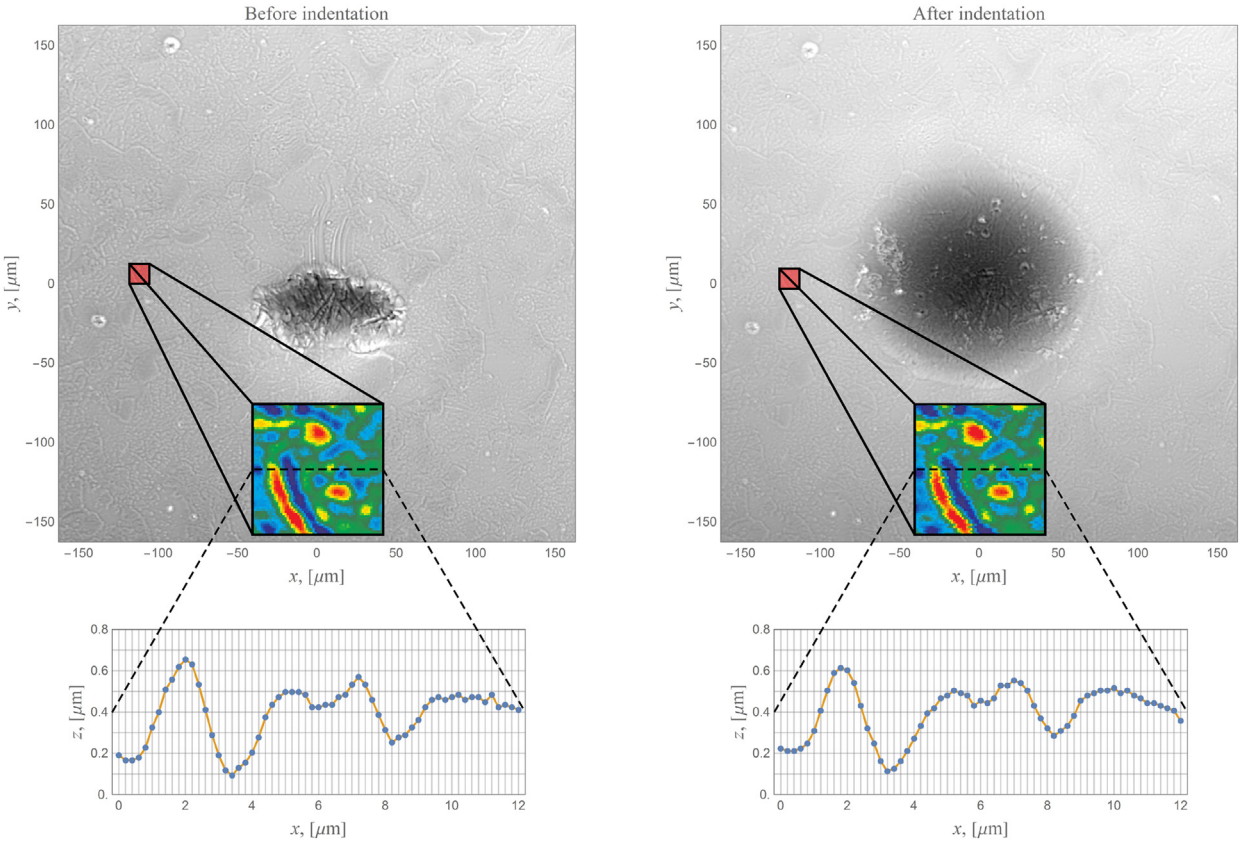

Fig. 4. The profiles (in grayscale representation) of the AISI 1040 disk before (left side) and after (right side) the indentation test. A portion of a specific area is highlighted (red semitransparent box) and magnified (color density box) in both configurations. In the lower row of the figure, the topography along the horizontal centerline of the highlighted area is represented with a further magnification, and the location of sampling points are evidenced by the vertical grid lines. (For interpretation of the references to color in this figure legend, the reader is referred to the web version of this article.)

to see the vertical translation stage, the microscope objective and the indenter of the hardness tester. The diameter of indentation resulted to be approximately 125 μm, with a consequent hardness equal to 162 HB, in accordance with what expected from this specific material. The use of an hardness machine, which is different from the micro- or nano-tester present on the profilometer station, was intentional, in order to demonstrate the capability of the procedure to retrieve the displacement field of any specimen. The author wants to prove the robustness of the procedure, which does not require all the steps of investigation under the machine to be carried out, as it is often required when high sensitivity measurement procedures are applied.

For this specimen a square ROI of 400 μm × 400 μm was chosen, and it was sampled by 2000 × 2000 acquisitions with the same value of δ fixed for the first specimen (0.2 μm). Consequently, in this case, the acquisition time was four times longer. Fig. 4 shows the surface profile of the AISI 1040 specimen acquired before (left side) and after (right side)

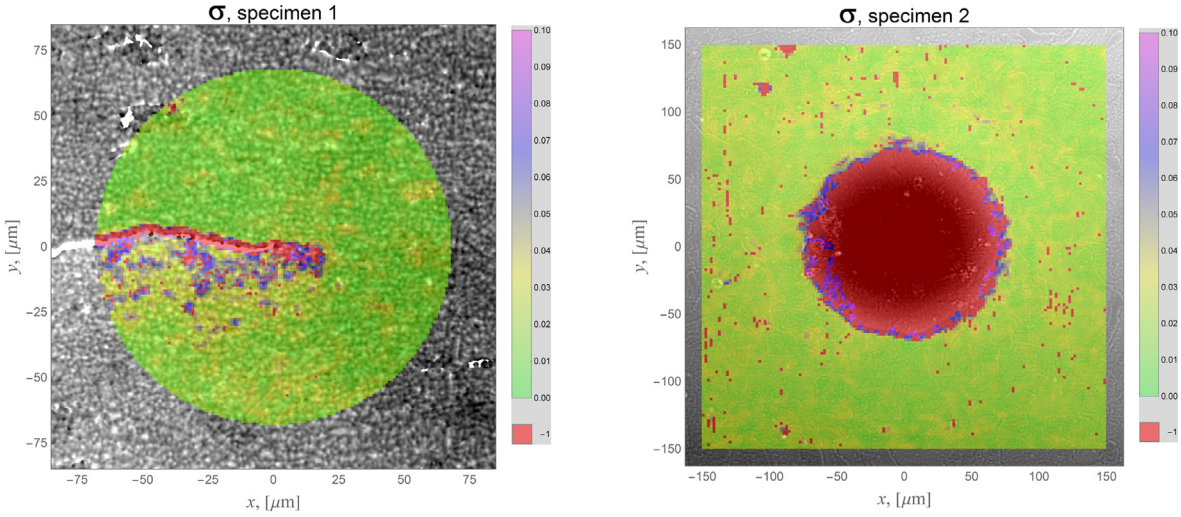

Fig. 5. Correlation coefficient distribution on the ROIs for the Ni-alloy specimen (left) and AISI 1040 specimen (right). The red dots represent the points where the correlation algorithm fails ($\sigma = -1$). (For interpretation of the references to color in this figure legend, the reader is referred to the web version of this article.)

the indentation test. In order to mark the ROI for this experiment, a superficial scratch visible on the left side of Fig. 4 was manually made before the execution of the indentation. The layout of the figure is the same as in Fig. 3, the only difference is that in this case the horizontal and vertical scales are doubled. The highlighted area was chosen to be 12 μm × 12 μm, i.e. 60 pixels × 60 pixels. Again, the roughness parameters are calculated and shown in Table 1.

For both specimens the DIC analyses were carried out assuming a subset of 21 pixels × 21 pixels, i.e. the correlation area around each pixel for which the displacement is calculated is 4 μm. For the two specimens, the step was assumed equal to 5 and 10 pixels, respectively, i.e. 40,000 points were analyzed in each case. For each of these points, the DIC algorithm extracts the two in-plane displacement components $u(x,y)$ and $v(x,y)$, and the correlation coefficient σ. All of these parameters are associated to each analyzed point by its spatial coordinates (x,y). The correlation coefficient σ assumes a value in the range [0;0.1] when a search for the point in the deformed configuration is successful, while a value −1 is assigned if it fails.

Subsequently, the out-of-plane component $w(x,y)$ is retrieved by exploiting the topographic information of the two loading configurations. By indicating with $h_0(x,y)$ and $h_1(x,y)$ the z-coordinate in the reference and deformed configuration, respectively, the function $w(x,y)$ can be evaluated as:

$$w(x,y) = h_1(x + u(x,y), y + v(x,y)) - h_0(x,y). \tag{1}$$

By applying Eq. (1), the out-of-plane component is assigned at the generic point in the reference configuration, consistently with the DIC algorithm. It is worth noting that the in-plane components evaluated by the 2D-DIC procedure are real numbers. On the other hand, the evaluation of $h_1(x,y)$ requires the definition of the profile at any point (x,y), not just in correspondence of the point whose z-coordinate is measured by the profilometer. Therefore it is necessary to interpolate the profile in the deformed configuration, in order to obtain a continuous function for the topography at any point of coordinates (x,y). This is an easy operation performed by any software for post-processing data.

After the three functions $u(x,y)$, $v(x,y)$, and $w(x,y)$ are determined, it would be possible, if necessary, to extract the six strain components by differentiating them. As these functions can be evaluated on the outer surface of the investigated specimen, they will only depend on the spatial variables x and y. Therefore, derivatives with respect to the z-coordinate cannot be performed. In the specific case of small displacement (conditions for any elastic displacement field are met, and the same case is also in the presence of moderate plastic deformations), the differential relationship between strain and displacement components is the following:

$$\varepsilon_x = \frac{\partial u}{\partial x} \quad \varepsilon_y = \frac{\partial v}{\partial y} \quad \gamma_{xy} = \frac{\partial u}{\partial y} + \frac{\partial v}{\partial x}, \tag{2}$$

$$\varepsilon_z = \frac{\partial w}{\partial z} \quad \gamma_{yz} = \frac{\partial v}{\partial z} + \frac{\partial w}{\partial y} \quad \gamma_{zx} = \frac{\partial w}{\partial x} + \frac{\partial u}{\partial z}. \tag{3}$$

The first three strain components (ε_x, ε_y, γ_{xy}) can be evaluated with the information provided by the method, while the longitudinal deformation along z direction (ε_z), by contrast, cannot. The other two shear strains (γ_{yz}, γ_{zx}) can be partially calculated, given the two derivatives with the respect of z. Nonetheless, the two derivatives $\partial w/\partial y$ and $\partial w/\partial x$ have a specific physical meaning. In fact, if at the location (x,y) the local normal is oriented along the z direction – i.e. planar surface – they represent the rotations of the normal around the x and y axes, respectively.

A final consideration on the method, regarding the intensity (proportional to the z-coordinate) distribution of the images to be processed. Depending on the robustness of the DIC algorithm adopted, a pre-processing operation could be necessary before running the correlation procedure. If the images do not provide a recognizable grain, the correlation algorithm has not identified the features necessary to quantify the displacement components. Many image processing operations might be applied to the images in order to obtain a better local contrast, which increases chances of convergence of the DIC procedure. In the specific case of the present method, it is important to keep in mind that the pixels' intensity is proportional to the local z-coordinate, which is necessary to retrieve the out-of-plane component by means of Eq. (1). Hence, any pre-processing operation applied to the images prior to a search for in-plane components by the DIC algorithm should be used only in the first step of the procedure. Subsequently, the original information – i.e. the topography of the specimens measured at the beginning – will necessarily be used for the following steps of the procedure.

3. Results and discussion

The feasibility of the proposed procedure is strictly dependent on the correlation level occurring among the images analyzed by the DIC procedures. Therefore, the analysis of the correlation coefficient σ is definitely a reliable test to evaluate the effectiveness of the method. Fig. 5 shows the distribution of σ on the ROI chosen for the two specimens.

In particular, for the first specimen, the ROI is a circle of 135 μm diameter, whose center was fixed at the crack tip. As it is usual in the analysis of the deformations in the fracture mechanics problems, the displacement field is studied by a polar domain centered on this point. The diameter of the circle is significantly smaller than the original domain acquired for this specimen (square area 200 μm × 200 μm) because of the in-plane rigid body motion, due to two effects. The first one depends on the reposition capability of the profilometer's scanning stage, which theoretically should be able to scan exactly the same portion of the specimen when the topography is measured two (or more) consecutive times, if nothing is moved under the machine. Obviously, the accuracy of the reposition operation depends on the scanning stage's precision, hysteresis, and linearity. The second effect comes from the application of the load, which should be very limited thanks to the specific type of the stage adopted, but obviously not perfectly zero, also because of the non-perfect central location of the crack along the loading direction. By observing the σ distribution on the first specimen (Fig. 5, left side), it is possible to notice that the DIC procedure works on most of the points, i.e. σ falls between 0 (perfect correlation, green points) and 0.1 (acceptance limit fixed by the DIC algorithm, purple points). The correlation procedure fails only on 527 (red points) over 14,530 points, which represent just the 3.6% of the total. Most of the failures occur around the crack tip, where the plastic deformations change deeply the roughness, and along the crack front, where the local rotations (around all the three axes) are more significant.

For the second specimen, the ROI was a 300 μm × 300 μm square, centered on the circle representing the indentation. Also in this case, part of the original domain was lost (square area 400 μm × 400 μm), again for two reasons associated with the rigid body motions. The first one is again the accuracy of the repositioning operation. On the other hand, the second reason is different from the previous test, due to the quite different type of mechanical test performed on this specific specimen. As mentioned in the previous section, the hardness test was executed on a different machine, not present on the testing station equipped with the confocal microscope used as profilometer. Hence, after the acquisition of the topography in the reference condition (before the execution of the indention), the specimen was moved under the hardness machine. Subsequently, after executing the indentation, the specimen was moved back under the profilometer, and the topography in the deformed condition was acquired. This procedure implies a manual moving, which introduces non negligible rigid body motions, mostly rotations around all the three axes. In this case, over 22,500 points of the ROI, 4191 points show a correlation coefficient equal to −1, which represent the 18.6% of the total. Nevertheless, the results

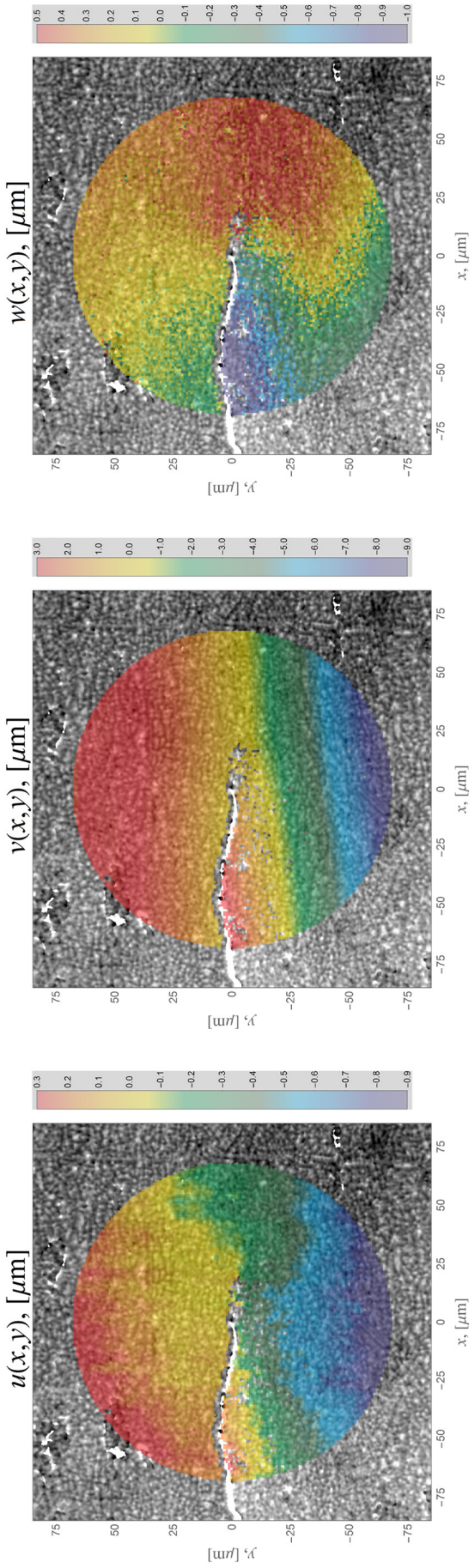

Fig. 6. Row data of the three displacement components obtained for the specimen 1, Ni-alloy edge crack thin plate subjected to a tensile test.

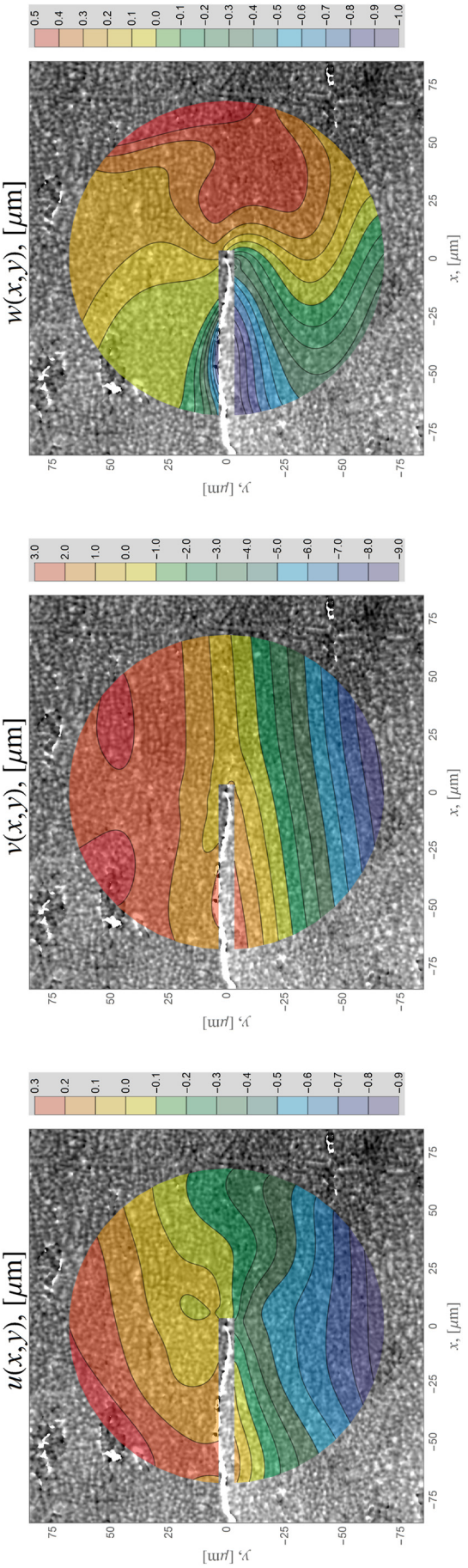

Fig. 7. Fitted maps for the three displacement components obtained for the specimen 1, Ni-alloy edge crack thin plate subjected to a tensile test.

obtained by this test should not be considered much worse than the previous one. As shown in the σ map for this specimen (Fig. 5, right side), all the points in the indentation area did not reach the correlation goal. This is due to the high plastic deformation imposed to the material during the hardness test. By a morphological operation performed on the σ values, the radius of the circle that best fits the indentation was estimated equal to 320 pixels, inside which fall 3140 points (over 3224) with a correlation coefficient equal to −1. Hence the actual number of points whose correlation coefficient resulted to be equal to −1 is 1051, which are the 5.4% of the total points.

Also by removing the points falling inside the indentation area, the specimen 2 shows a little more (in percentage) information to be discarded, if compared with the specimen 1 (5.4% against 3.6%). This fact is mostly due to the significant difference of roughness, as shown by Table 1. A higher value of roughness, as in the case of specimen 1, gives to the images obtained from the topography an easier structure to be recognized from the correlation algorithm. In contrast, the reduced value of the *z*-coordinates of a smoother surface makes the different areas of the specimen topography more similar among them, with a consequent higher probability for the search procedure to fail. Nevertheless, even with a highly polished surface, as in the case of specimen 2, about a twentieth of the total points give non reliable information, which still represents a profitable working condition when the mechanical deformations are measured by DIC techniques.

The raw data of the three displacement components for the first specimen are reported in Fig. 6. The three density plots were obtained by representing a square of the proper color (according to the bar associated to each graph), with the side equal to the step (5 pixels), and centered on the pixel for which the displacement components are calculated. In particular, it is worth mentioning again that the two in-plane components $u(x,y)$ and $v(x,y)$ were evaluated by the correlation algorithm, while the out-of-plane components $w(x,y)$ was calculated by applying Eq. (1), which requires the knowledge at any point (x,y) of the results of the DIC and topographic analyses, i.e. $u(x,y)$, $v(x,y)$, $h_0(x,y)$ and $h_1(x,y)$. The displacement components were represented on all the points where σ resulted to be different from −1.

As shown in Fig. 6, the displacement maps resulted to be enough regular for a preliminary study of the mechanical deformation field, that is a further confirmation of the effectiveness of the proposed method. On the other hand, some specific analyses could require more refined operations on the displacement fields, hence smoother spatial distributions for displacement components would be more helpful. The fitting of the fields shown in Fig. 6 was performed by the method proposed by the author in [55], which allows managing discontinuities within the fitting domain. The circular domain was described in polar coordinates by B-spline forth order functions – i.e. cubic polynomials – by using 12 control points along the angular coordinate and 5 along the radial one. The results of the fitting operation is shown in Fig. 7, where the contour maps of the three displacement components are represented using the same color bar of Fig. 6.

The fitting operation is based on a linear optimization process of the squared errors, therefore the mean value of the random variables *ex*, *ey*, and *ez* (calculated for each component as the difference at any point between the experimental value and the analytical one) is exactly equal to zero. Instead, the standard deviation of these functions – i.e. the mean squared error (MSE) – provides a measurement of the dispersion of the experimental data around the best-fit surface. The MSEs for the three displacement components resulted equal to 27 nm, 44 nm and 16 nm for $u(x,y)$, $v(x,y)$ and $w(x,y)$, respectively. The distributions of the random variables can be considered Gaussian with good approximation, as shown in Fig. 8, where the histograms represent the distribution of *ex*, *ey*, and *ez*, and the continuous line is a theoretical normal distribution with zero mean and the same standard deviation of the corresponding experimental data.

The same results are reported for the specimen 2. Fig. 9 shows the raw data for the three displacement components, in this case the step used in the DIC analysis was equal to 10 pixels.

Also in this case, the experimental data were fitted and a different procedure was adopted [56], in order to take into account the lack of information on the indentation area. Again, cubic polynomials were used, and 7×7 control points allowed obtaining a proper analytical function for modeling the displacement fields on the whole domain. Fig. 10 shows the three fitted displacement components. Thanks to the regularity of the displacement field, a little extrapolation was carried out in the outer part of the indentation area (about 10% of the radius corresponding to about 20% of the area). It is possible to notice that the rigid body motion implied from this type of test is not negligible, as in the case of the previous one. In fact, the repositioning operation of the specimen after the execution of the indentation was carried out manually, hence the rotations around the three axes cannot be compensated without using all the three displacement components, which are available only after the application of the whole procedure.

Fig. 11 shows the three displacement components after the application a compensation procedure of the rigid body motion. The two in-plane translations and the rotation around the normal were evaluated by the function $u(x,y)$ and $v(x,y)$, while by $w(x,y)$ the out-of-plane translation and the two rotations around the in-plane axes were calculated.

Finally, the experimental data and the fitting model were used for quantifying the scattering of the measurements carried out by the proposed method. As in the case of specimen 1, the three random variables *ex*, *ey*, and *ez* were calculated, and the MSEs resulted equal to 102 nm, 36 nm and 8 nm, respectively. The value of MSE was significantly higher in the case of the displacement component $u(x,y)$. This axis is the one used by the translation stage for moving the specimen among the different machines of the measurement station – i.e. the optical microscope, the profilometer, the micro- and the nano-indenter – and it could be affected from the highest miscalibration (Fig. 12).

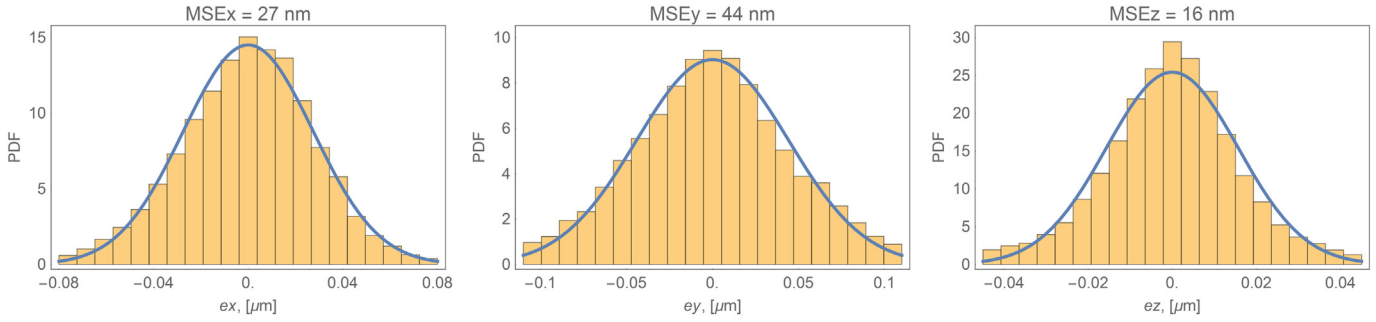

Fig. 8. Specimen 1: distribution of the error random variables *ex*, *ey* and *ez*, for the three displacement components, calculated as the difference between the experimental data and the analytical values provided by the model obtained after the fitting operation. The histograms represent the errors, the continuous lines are normal distributions with same (zero) mean and standard deviation of the error random variables.

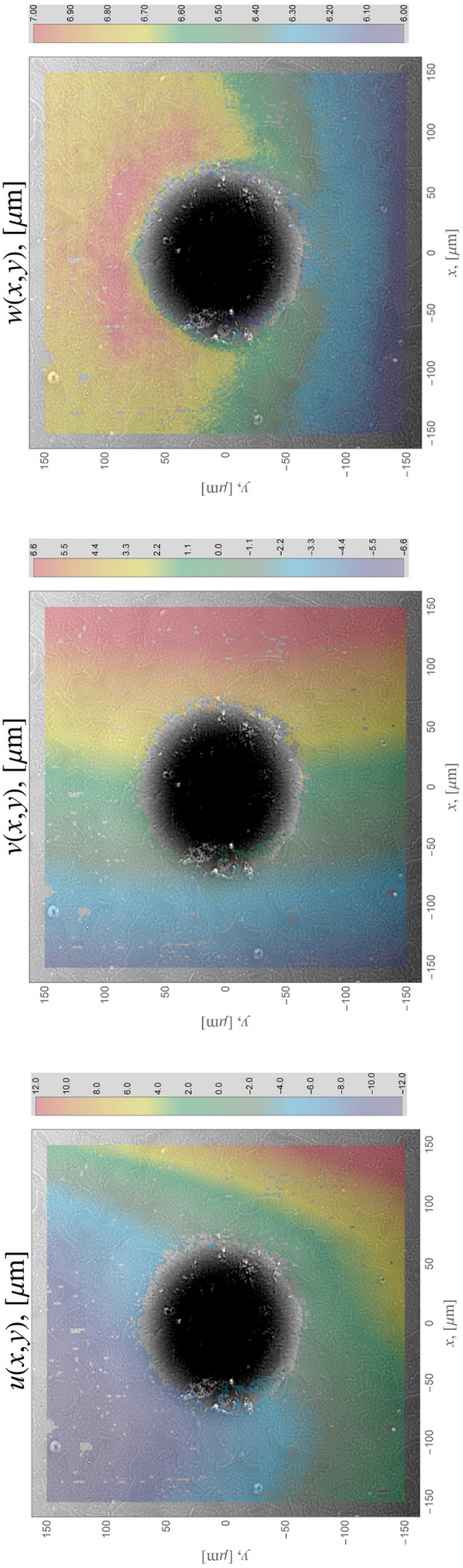

Fig. 9. Row data of the three displacement components obtained for the specimen 2, AISI 1040 subjected to a hardness test.

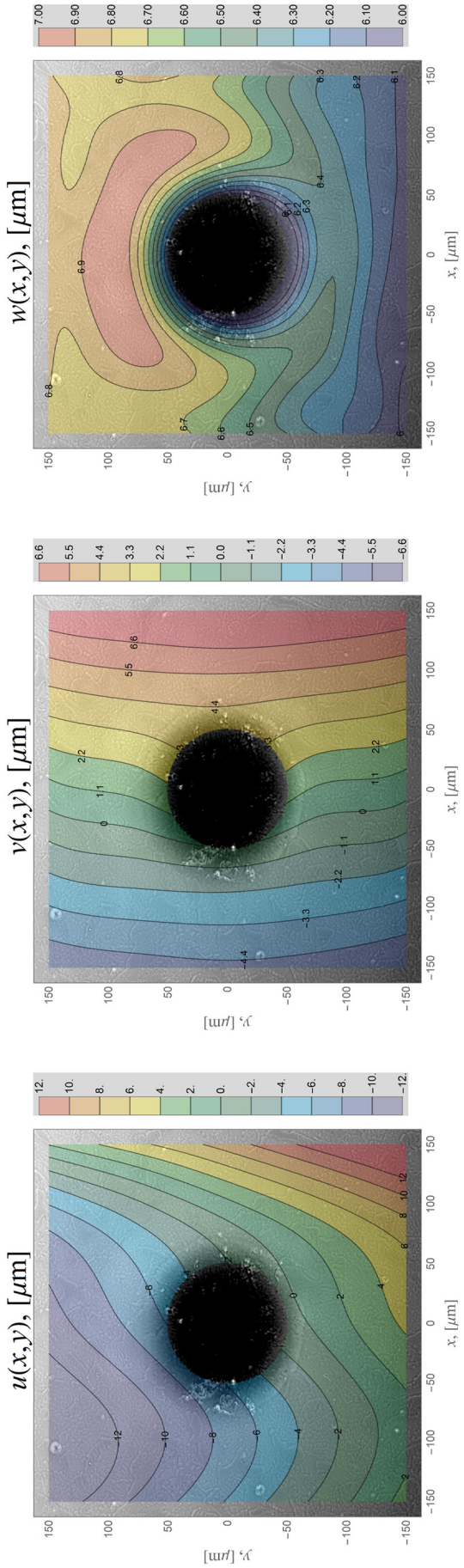

Fig. 10. Fitted maps for the three displacement components obtained for the specimen 2, AISI 1040 subjected to a hardness test.

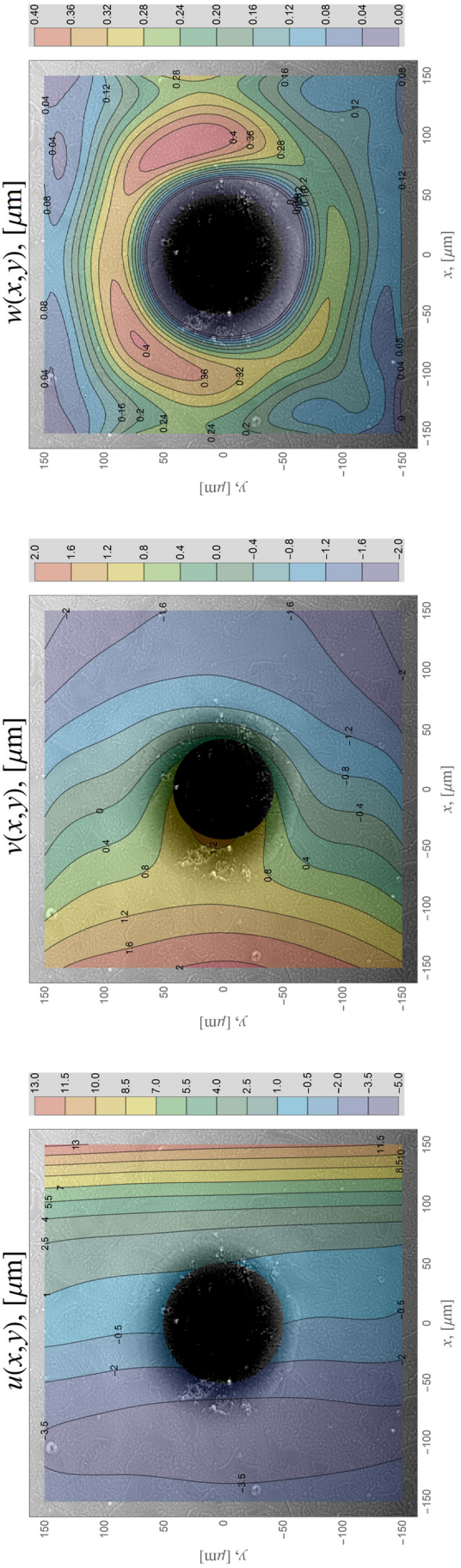

Fig. 11. Fitted maps for the three displacement components obtained for the specimen 2 after the compensation of the rigid body motion.

4. Conclusions

This manuscript describes in detail a method which allows for the measurement of the entire displacement vector field within a small area, the topography of which is retrieved in two different deformed configurations using any method – e.g. white light interferometry, confocal microscopy, atomic force microscopy. The in-plane displacement components are measured by the application of a conventional DIC algorithm, which identifies the corresponding areas in the two configurations by correlating the 3D profiles. The out-of-plane component is determined by comparing the *z*-coordinate of the two configurations between the two corresponding points identified by the DIC algorithm.

The procedure was successfully applied in two case studies by means of Confocal Microscopy (CM): an edge crack Ni-alloy specimen subjected to a tensile test and a hardness test performed on high carbon steel. An analysis of the correlation coefficient demonstrated that the method can work in the presence of an ordinary engineering roughness (Ni-alloy specimen) or in that of a highly polished surface for metallographic application (steel specimen). For both specimens, raw and fitted data were displayed, and the noise was quantified by a proper statistical analysis.

The investigated areas were equal to hundreds of square-micrometers (150 μm × 150 μm and in the first experiment, 300 μm × 300 μm in the second) and the accuracy attained by the proposed method was equal to 10 nm on all three of the displacement components. This is better than that obtained through stereo-DIC methods and sufficient for several applications in the field of mechanics of materials – e.g. residual stresses by semi-destructive and destructive methods, mechanical characterization at macro- and micro-scale, and monitoring of strain relief around macro-, micro- and nano-indentation. The extension of these areas could be even bigger, provided that the acquisition time for the experiments is compatible. If smaller areas need to be investigated, or if a better accuracy is required, similar approaches can be used, but some modifications to the hardware equipment and software procedures should be applied, as shown in other applications discussed in the introduction [36–41,43–49].

The most significant strengths of the method can be summarized in the following points.

- *Simple input data*. The experimental data set necessary to retrieve all the displacement components is very simple, i.e. the topography of the portion of surface under investigation in two (or more) loading configurations.
- *High sensitivity*. For the in-plane components, sensitivity depends on the accuracy of the scanning system, while for the out-of-plane component it depends on the accuracy of the profile measurement. Usually, these are accurate to within a few nanometers, but sub-nanometric precisions can be reached by many devices.
- *Straightforward procedure*. The correlation procedure for in-plane components and the calculation of the out-of-plane component by means of DIC and profile data do not require a complex search method, such as non-linear optimization or genetic algorithm, which in many circumstances could imply significant error and/or long calculation times.
- *Error on z component independent from the scan error*. Possible inaccuracy occurring during the scan of the surface will not affect evaluation of the *z* component, due to the fact that the correlation procedure identifies the same point in all the loading configurations analyzed by the DIC analysis.
- *Software integration*. The procedure can be easily integrated into software that manages a profilometer. Simple post-processing modules can be added for performing the most important steps of the procedure – e.g. definition of region of interest, subset and step; visualization of the results; compensation of rigid body motions; filtering and smoothing the displacement field; exporting results.

On the other hand, some limitations could arise from the application of the method.

- *Slow experimental data acquisition*. The acquisition of the experimental data necessary to apply the procedure is intrinsically slow, due to the scanning operation normally required by the profilometer. Nevertheless, technological progress is continuously diminishing the acquisition time, and today some machines can also provide full-field one-shot acquisition, the accuracy of which is the object of ongoing study and development.
- *Inaccuracy due to the scanning operation*. The scan of the surface under investigation is normally performed by high-resolution translation stages, often based on closed-loop piezoelectric actuators. Non-linearity, hysteresis, miscalibration errors imply inaccuracy in the determination of the in-plane components evaluated by the DIC procedure. Zero tests, based on the repeated acquisition of the same surface without applying any deformation field, can be useful for characterizing this possible source of inaccuracy.
- *Presence of rigid body motions*. Due to the load application system, specimens often suffer non-negligible rigid body motions, which can obscure information contained in the displacement field. Such motions should therefore be compensated by proper procedures.
- *Difficulty in analyzing non-planar surfaces*. The topography acquisition implies a measurement of both the micro- and macro-features of the surface being tested. A non-planar surface contains micro-features due to its roughness (that represents the method's basic carrier of information) and macro-features due to its geometry. These macro-features could require a measurement range much higher than that necessary for retrieving roughness features. A

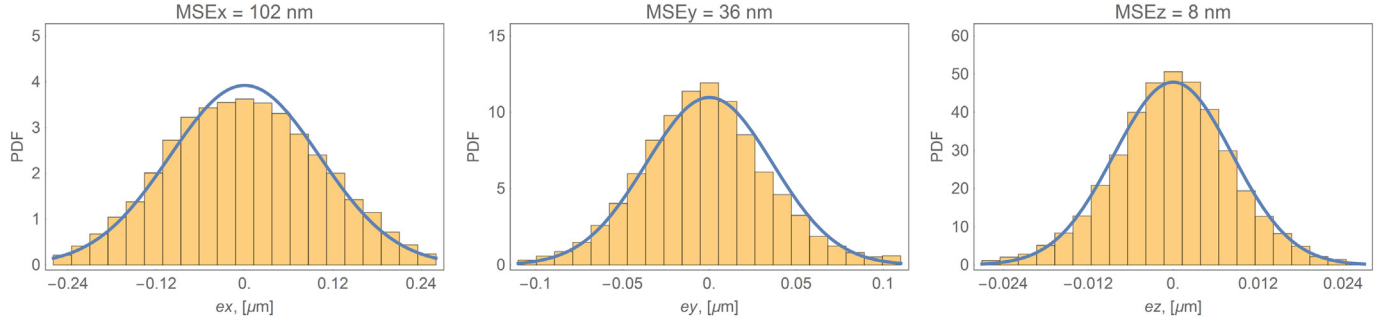

Fig. 12. Specimen 2: distribution of the error random variables *ex*, *ey* and *ez*, for the three displacement components, calculated as the difference between the experimental data and the analytical values provided by the model obtained after the fitting operation. The histograms represent the errors, the continuous lines are normal distributions with same (zero) mean and standard deviation of the error random variables.

higher range normally implies lower accuracy on the *z*-coordinate measurement, creating consequent accuracy concerns for both in-plane and out-of-plane components.

— *Inability to correlate the point in the presence of high deformation.* As shown in the second case study, when deformations are too high, excessive distortion of the local structure implies a failure of the correlation algorithm. The issue could be totally or partially corrected if an incremental measurement of the displacement field can be carried out while strains on the investigated area are being developed.

Acknowledgments

I want to thank my mentor, Prof. Andrea Poggialini, for having awakened in me a passion for teaching and research. Without him, I would have never been the professor or the engineer that I am today. I want to thank my wife, Eva, for her patience in editing all my papers, for supporting any project I undertake, and for the unconditional love that she provides to me daily.

References

[1] J. Rasson, O. Poncelet, S.R. Mouchet, O. Deparis, L.A. Francis, Vapor sensing using a bio-inspired porous silicon photonic crystal, Mater. Today Proc. 4 (2017) 5006–5012, https://doi.org/10.1016/j.matpr.2017.04.107.
[2] Y. Han, S. Li, F. Chen, T. Zhao, Multi-scale alignment construction for strong and conductive carbon nanotube/carbon composites, Mater. Today Commun. 6 (2016) 56–68, https://doi.org/10.1016/j.mtcomm.2015.12.002.
[3] S. Brundavanam, R.K. Brundavanam, G.E.J. Poinern, D. Fawcett, Flower-like Brushite structures on mg, Mater. Today 20 (2017) 92–93, https://doi.org/10.1016/j.mattod.2017.01.014.
[4] P. Parandoush, D. Lin, A review on additive manufacturing of polymer-fiber composites, Compos. Struct. 182 (2017) 36–53, https://doi.org/10.1016/j.compstruct.2017.08.088.
[5] G. Dehm, B.N. Jaya, R. Raghavan, C. Kirchlechner, Overview on micro- and nanomechanical testing: new insights in interface plasticity and fracture at small length scales, Acta Mater. 142 (2018) 248–282, https://doi.org/10.1016/j.actamat.2017.06.019.
[6] W.S.W. Harun, R.I.M. Asri, J. Alias, F.H. Zulkifli, K. Kadirgama, S.A.C. Ghani, J.H.M. Shariffuddin, A comprehensive review of hydroxyapatite-based coatings adhesion on metallic biomaterials, Ceram. Int. 44 (2018) 1250–1268, https://doi.org/10.1016/j.ceramint.2017.10.162.
[7] C.H. Nguyễn, J.-L. Putaux, G. Santoni, S. Tfaili, S. Fourmentin, J.-B. Coty, L. Choisnard, A. Gèze, D. Wouessidjewe, G. Barratt, S. Lesieur, F.-X. Legrand, New nanoparticles obtained by co-assembly of amphiphilic cyclodextrins and nonlamellar single-chain lipids: preparation and characterization, Int. J. Pharm. 531 (2017) 444–456, https://doi.org/10.1016/j.ijpharm.2017.07.007.
[8] J. Lee, M. Morita, K. Takemura, E.Y. Park, A multi-functional gold/iron-oxide nanoparticle-CNT hybrid nanomaterial as virus DNA sensing platform, Biosens. Bioelectron. 102 (2018) 425–431, https://doi.org/10.1016/j.bios.2017.11.052.
[9] A.F. Doval, A systematic approach to TV holography, Meas. Sci. Technol. 11 (2000) R1–R36, https://doi.org/10.1088/0957-0233/11/1/201.
[10] W. Osten, A. Faridian, P. Gao, K. Körner, D. Naik, G. Pedrini, A.K. Singh, M. Takeda, M. Wilke, Recent advances in digital holography [invited], Appl. Opt. 53 (2014) G44–G63, https://doi.org/10.1364/AO.53.000G44.
[11] M.A. Sutton, J.-J. Orteu, H.W. Schreier, Image Correlation for Shape, Motion and Deformation Measurements, Springer-Verlag, New York, 2009https://doi.org/10.1007/978-0-387-78747-3.
[12] G. Binnig, H. Rohrer, Scanning tunneling microscopy, Surf. Sci. 126 (1983) 236–244, https://doi.org/10.1016/0039-6028(83)90716-1.
[13] G. Binnig, C.F. Quate, C. Gerber, Atomic force microscope, Phys. Rev. Lett. 56 (1986) 930–933, https://doi.org/10.1103/PhysRevLett.56.930.
[14] L. Deck, P. De Groot, High-speed noncontact profiler based on scanning white-light interferometry, Appl. Opt. 33 (1994) 7334–7338, https://doi.org/10.1364/AO.33.007334.
[15] B.S. Lee, T.C. Strand, Profilometry with a coherence scanning microscope, Appl. Opt. 29 (1990) 3784–3788, https://doi.org/10.1364/AO.29.003784.
[16] J. Schwerdtfeger, E. Nadgorny, V. Koutsos, J.R. Blackford, M. Zaiser, Statistical heterogeneity of plastic deformation: an investigation based on surface profilometry, Acta Mater. 58 (2010) 4859–4870, https://doi.org/10.1016/j.actamat.2010.05.024.
[17] S.F.S.P. Looijmans, P.D. Anderson, L.C.A. van Breemen, Contact mechanics of isotactic polypropylene: effect of pre-stretch on the frictional response, Wear 398–399 (2018) 183–190, https://doi.org/10.1016/j.wear.2017.12.002.
[18] V.I. Betekhtin, A.G. Kadomtsev, M.V. Narykova, M.V. Bannikov, S.G. Abaimov, I.S. Akhatov, T. Palin-Luc, O.B. Naimark, Experimental and theoretical study of multiscale damage-failure transition in very high cycle fatigue, Phys. Mesomech. 20 (2017) 78–89, https://doi.org/10.1134/S1029959917010076.
[19] R. Fontana, A. Dal Fovo, J. Striova, L. Pezzati, E. Pampaloni, M. Raffaelli, M. Barucci, Application of non-invasive optical monitoring methodologies to follow and record painting cleaning processes, Appl. Phys. A Mater. Sci. Process. 121 (2015) 957–966, https://doi.org/10.1007/s00339-015-9505-5.
[20] M. Schätzle, S. Zinelis, G. Markic, G. Eliades, T. Eliades, Structural, morphological, compositional, and mechanical changes of palatal implants after use: a retrieval analysis, Eur. J. Orthod. 39 (2017) 579–585, https://doi.org/10.1093/ejo/cjx001.
[21] J. Kang, D.S. Wilkinson, J.D. Embury, M. Jain, Microscopic strain mapping using scanning electron microscopy topography image correlation at large strain, J. Strain Anal. Eng. Des. 40 (2005) 559–570, https://doi.org/10.1243/030932405X16151.
[22] M.A. Tschopp, B.B. Bartha, W.J. Porter, P.T. Murray, S.B. Fairchild, Microstructure-dependent local strain behavior in polycrystals through in-situ scanning electron microscope tensile experiments, Metall. Mater. Trans. A Phys. Metall. Mater. Sci. 40 (2009) 2363–2368, https://doi.org/10.1007/s11661-009-9938-6.
[23] C.C. Tasan, J.P.M. Hoefnagels, M.G.D. Geers, Microstructural banding effects clarified through micrographic digital image correlation, Scr. Mater. 62 (2010) 835–838, https://doi.org/10.1016/j.scriptamat.2010.02.014.
[24] H. Bi, C. Jang, B. Han, Nano-pattern recognition and correlation technique for sub-nanometer in-plane displacement measurement, Exp. Mech. 50 (2010) 1169–1181, https://doi.org/10.1007/s11340-010-9332-8.
[25] L.I.J.C. Bergers, J.P.M. Hoefnagels, M.G.D. Geers, On-wafer time-dependent high reproducibility nano-force tensile testing, J. Phys. D. Appl. Phys. 47 (2014)https://doi.org/10.1088/0022-3727/47/49/495306.
[26] J.C. Pina, S. Shafqat, V.G. Kouznetsova, J.P.M. Hoefnagels, M.G.D. Geers, Microstructural study of the mechanical response of compacted graphite iron: an experimental and numerical approach, Mater. Sci. Eng. A 658 (2016) 439–449, https://doi.org/10.1016/j.msea.2016.02.017.
[27] J.C. Stinville, M.P. Echlin, D. Texier, F. Bridier, P. Bocher, T.M. Pollock, Sub-grain scale digital image correlation by electron microscopy for polycrystalline materials during elastic and plastic deformation, Exp. Mech. 56 (2016) 197–216, https://doi.org/10.1007/s11340-015-0083-4.
[28] X. Wang, Z. Pan, F. Fan, J. Wang, Y. Liu, S.X. Mao, T. Zhu, S. Xia, Nanoscale deformation analysis with high-resolution transmission electron microscopy and digital image correlation, J. Appl. Mech. 82 (2015)https://doi.org/10.1115/1.4031332.
[29] J. Jiang, J. Yang, T. Zhang, J. Zou, Y. Wang, F.P.E. Dunne, T.B. Britton, Microstructurally sensitive crack nucleation around inclusions in powder metallurgy nickel-based superalloys, Acta Mater. 117 (2016) 333–344, https://doi.org/10.1016/j.actamat.2016.07.023.
[30] C. Sun, B. Standish, B. Vuong, X.-Y. Wen, V. Yang, Digital image correlation-based optical coherence elastography, J. Biomed. Opt. 18 (2013)https://doi.org/10.1117/1.JBO.18.12.121515.
[31] H. Tran, J. Grimm, B. Wang, M.A. Smith, A. Gogola, S. Nelson, E. Tyler-Kabara, J. Schuman, G. Wollstein, I.A. Sigal, Mapping in-vivo optic nerve head strains caused by intraocular and intracranial pressures, Prog. Biomed. Opt. Imaging, Proc. SPIE, San Francisco CA, 2017, 100670B. https://doi.org/10.1117/12.2257360.
[32] J. Fu, M. Haghighi-Abayneh, F. Pierron, P.D. Ruiz, Assessment of corneal deformation using optical coherence tomography and digital volume correlation, in: B.C. Prorok, F. Barthelat, C.S. Korach, K.J. Grande-Allen, E. Lipke, G. Lykofatitits, P. Zavattieri (Eds.), Annu. Conf. Exp. Appl. Mech, Springer New York, New York, NY 2013, pp. 155–160.
[33] G. Vendroux, W.G. Knauss, Submicron deformation field measurements: part 1. Developing a digital scanning tunneling microscope, Exp. Mech. 38 (1998) 18–23.
[34] G. Vendroux, W.G. Knauss, Submicron deformation field measurements: part 2. Improved digital image correlation, Exp. Mech. 38 (1998) 86–92.
[35] G. Vendroux, N. Schmidt, W.G. Knauss, Submicron deformation field measurements: part 3. Demonstration of deformation determinations, Exp. Mech. 38 (1998) 154–160.
[36] X. Li, W. Xu, M.A. Sutton, M. Mello, In situ nanoscale in-plane deformation studies of ultrathin polymeric films during tensile deformation using atomic force microscopy and digital image correlation techniques, IEEE Trans. Nanotechnol. 6 (2007) 4–12, https://doi.org/10.1109/TNANO.2006.888527.
[37] Z.-H. Xu, X.-D. Li, M.A. Sutton, N. Li, Drift and spatial distortion elimination in atomic force microscopy images by the digital image correlation technique, J. Strain Anal. Eng. Des. 43 (2008) 729–743, https://doi.org/10.1243/03093247JSA400.
[38] Z.-H. Xu, M.A. Sutton, X. Li, Mapping nanoscale wear field by combined atomic force microscopy and digital image correlation techniques, Acta Mater. 56 (2008) 6304–6309, https://doi.org/10.1016/j.actamat.2008.08.044.
[39] J. Araujo de Oliveira, J. Kowal, S. Gungor, M.E. Fitzpatrick, Determination of normal and shear residual stresses from fracture surface mismatch, Mater. Des. 83 (2015) 176–184, https://doi.org/10.1016/j.matdes.2015.06.014.
[40] S. Cho, J.F. Cárdenas-García, I. Chasiotis, Measurement of nanodisplacements and elastic properties of MEMS via the microscopic hole method, Sensors Actuators A Phys. 120 (2005) 163–171, https://doi.org/10.1016/j.sna.2004.11.028.
[41] K. Han, M. Ciccotti, S. Roux, Measuring nanoscale stress intensity factors with an atomic force microscope, EPL 89 (2010)https://doi.org/10.1209/0295-5075/89/66003.
[42] A. Baldi, F. Bertolino, Assessment of h-refinement procedure for global digital image correlation, Meccanica 51 (2016) 979–991, https://doi.org/10.1007/s11012-015-0253-6.
[43] J. van Beeck, J. Neggers, P.J.G. Schreurs, J.P.M. Hoefnagels, M.G.D. Geers, Quantification of three-dimensional surface deformation using global digital image correlation, Exp. Mech. 54 (2014) 557–570, https://doi.org/10.1007/s11340-013-9799-1.
[44] J. Van Beeck, L.C.A. Van Breemen, P.J.G. Schreurs, M.G.D. Geers, Preventing interface damage by pre-conditioning polymer-coated steels via rolling, Int. J. Solids Struct. 58 (2015) 1–11, https://doi.org/10.1016/j.ijsolstr.2014.12.007.
[45] J. Van Beeck, P.J.G. Schreurs, M.G.D. Geers, Numerical-experimental assessment of roughness-induced metal-polymer interface failure, Mech. Mater. 80 ((2015) 234–245, https://doi.org/10.1016/j.mechmat.2014.04.012.

[46] M. Bertin, C. Du, J.P.M. Hoefnagels, F. Hild, Crystal plasticity parameter identification with 3D measurements and Integrated Digital Image Correlation, Acta Mater. 116 (2016) 321–331, https://doi.org/10.1016/j.actamat.2016.06.039.
[47] S.M. Kleinendorst, J.P.M. Hoefnagels, R.C. Fleerakkers, M.P.F.H.L. van Maris, E. Cattarinuzzi, C.V. Verhoosel, M.G.D. Geers, Adaptive isogeometric digital height correlation: application to stretchable electronics, Strain 52 (2016) 336–354, https://doi.org/10.1111/str.12189.
[48] J. Neggers, J.P.M. Hoefnagels, F. Hild, S. Roux, M.G.D. Geers, Direct stress-strain measurements from bulged membranes using topography image correlation, Exp. Mech. 54 (2014) 717–727, https://doi.org/10.1007/s11340-013-9832-4.
[49] L.I.J.C. Bergers, J.P.M. Hoefnagels, M.G.D. Geers, Characterization of time-dependent anelastic microbeam bending mechanics, J. Phys. D. Appl. Phys. 47 (2014)https://doi.org/10.1088/0022-3727/47/35/355306.
[50] M.D. McMurtrey, B. Cui, I. Robertson, D. Farkas, G.S. Was, Mechanism of dislocation channel-induced irradiation assisted stress corrosion crack initiation in austenitic stainless steel, Curr. Opin. Solid State Mater. Sci. 19 (2015) 305–314, https://doi.org/10.1016/j.cossms.2015.04.001.
[51] Anton Paar, (n.d.).
[52] Correlated Solutions, Vic-2D, Vic-3D, (n.d.).
[53] S. Yaofeng, J.H.L. Pang, Study of optimal subset size in digital image correlation of speckle pattern images, Opt. Lasers Eng. 45 (2007) 967–974, https://doi.org/10.1016/j.optlaseng.2007.01.012.
[54] B. Pan, H. Xie, Z. Wang, K. Qian, Z. Wang, Study on subset size selection in digital image correlation for speckle patterns, Opt. Express 16 (2008) 7037–7048, https://doi.org/10.1364/OE.16.007037.
[55] L. Bruno, Global approach for fitting 2D interferometric data, Opt. Express 15 (2007) https://doi.org/10.1364/OE.15.004835.
[56] L. Bruno, Isoparametric fitting: a method for approximating full-field experimental data distributed on any shaped 3D domain, Opt. Lasers Eng. 87 (2015)https://doi.org/10.1016/j.optlaseng.2016.02.007.